PNAS RESEARCH ARTICLE | BIOPHYSICS AND COMPUTATIONAL BIOLOGY

Temporal and spatial resolution of distal protein motions that activate hydrogen tunneling in soybean lipoxygenase

Jan Paulo T. Zaragoza[a,b,1], Adam R. Offenbacher[a,b,c,1], Shenshen Hu[a,b], Christine L. Gee[a,d], Zachary M. Firestein[b], Natalie Minnetian[b], Zhenyu Deng[b], Flora Fan[b], Anthony T. Iavarone[a,b], and Judith P. Klinman[a,b,d,2]

Contributed by Judith P. Klinman; received July 6, 2022; accepted January 27, 2023; reviewed by Steven G. Boxer, Christopher M. Cheatum, Dorothee Kern, and David M. Leitner

The enzyme soybean lipoxygenase (SLO) provides a prototype for deep tunneling mechanisms in hydrogen transfer catalysis. This work combines room temperature X-ray studies with extended hydrogen–deuterium exchange experiments to define a catalytically-linked, radiating cone of aliphatic side chains that connects an active site iron center of SLO to the protein–solvent interface. Employing eight variants of SLO that have been appended with a fluorescent probe at the identified surface loop, nanosecond fluorescence Stokes shifts have been measured. We report a remarkable identity of the energies of activation (E_a) for the Stokes shifts decay rates and the millisecond C–H bond cleavage step that is restricted to side chain mutants within an identified thermal network. These findings implicate a direct coupling of distal protein motions surrounding the exposed fluorescent probe to active site motions controlling catalysis. While the role of dynamics in enzyme function has been predominantly attributed to a distributed protein conformational landscape, the presented data implicate a thermally initiated, cooperative protein reorganization that occurs on a timescale faster than nanosecond and represents the enthalpic barrier to the reaction of SLO.

thermal activation | hydrogen tunneling | hydrogen–deuterium exchange | Stokes shift decay | room temperature X-ray

Significance

Using a variety of biophysical tools, we present evidence of a cooperative protein restructuring that originates at a defined protein–water interface to provide the thermal activation driving the active site hydrogen tunneling in soybean lipoxygenase (SLO). An atomistic understanding of how classical motions within the protein scaffold may control the active site quantum properties becomes apparent when the substrate linoleic acid is modeled into available X-ray structures for SLO. A dynamical model of enzyme catalysis is presented that combines distributed conformational ensembles with site-specific thermal initiation of the chemical reaction.

The contribution of protein scaffold motions to the modulation of reaction barrier height and shape remains a major unresolved component in our ability to describe the physical properties underlying enzyme catalysis. The vast majority of enzyme-catalyzed reactions require thermal activation, with only a small handful of enzymes undergoing photochemical initiation (1–3). Temperature-dependent hydrogen–deuterium exchange coupled to mass spectrometry (TDHDX–MS) has recently emerged as a broadly accessible experimental tool to interrogate heat-induced changes in local protein flexibility, which when coupled to function-altering protein mutations provides time-averaged spatial resolution of activated networks that lead from protein–solvent interfaces to enzyme active sites (4–8). The growing identification of such reaction-specific networks that are distinctive from each other, and independent of protein scaffold conservation, points toward scaffold-embedded heat conduits as a source of dynamical activation in enzyme catalysis (9–16).

To explore how heat transfer from a protein–solvent interface to an enzyme active site may enable catalysis, we turned to soybean lipoxygenase (SLO), a paradigmatic enzyme for quantum mechanical tunneling in biological C–H bond cleavage reactions (17). SLO catalyzes the production of fatty acid hydroperoxides at (*Z,Z*)-1,4-pentadienoic moieties via a rate-limiting proton-coupled electron (net hydrogen atom) transfer from the reactive carbon (C11) of substrate to an Fe^{III}(OH) cofactor (Fig. 1*A*). The physiological substrate, 9,12-(*Z,Z*)-octadecadienoic acid (linoleic acid, LA), is converted to 13-(*S*)-hydroperoxy -9,11-(*Z,E*)-octadecadienoic acid (13-HPOD). The resulting oxygenated lipids and their by-products are essential for signaling structural and metabolic changes in the cell, including seed growth and plant development (18). Native SLO catalysis exhibits a fairly weak temperature dependence (E_a ~2.0 kcal/mol), a small Arrhenius prefactor ($A_H < 10^5\ s^{-1}$), and a greatly inflated kinetic isotope effect on k_{cat} ($^Dk_{cat}$ = 81) (19, 20) that rises to $^Dk_{cat}$ = 500 to 700 for an enzyme variant that has been mutated at two bulky hydrophobic side chains surrounding the reactive carbon of bound substrate (21). The aggregate structural and kinetic properties of SLO played a key role in the development of vibronically nonadiabatic analytical tunneling expressions (20, 22–26).

The extension of Marcus-like models for long-range electron tunneling to hydrogen transfer reactions provides a powerful formalism that accommodates the multidimensional properties of hydrogen tunneling at room temperature (20, 22, 23, 26–29). In particular, the resulting separation of the temperature-dependent protein environmental

Preprint Servers: This manuscript was deposited as a preprint at bioRxiv and can be accessed with the following DOI: 10.1101/2022.03.31.486235.

Author contributions: J.P.T.Z., A.R.O., and J.P.K. designed research; J.P.T.Z., A.R.O., S.H., C.L.G., Z.M.F., N.M., Z.D., F.F., and A.T.I. performed research; J.P.T.Z., A.R.O., and C.L.G. analyzed data; and J.P.T.Z., A.R.O., and J.P.K. wrote the paper.

Reviewers: S.G.B., Stanford University; C.M.C., The University of Iowa; D.K., Brandeis University; and D.M.L., University of Nevada, Reno.

The authors declare no competing interest.

[1]J.P.T.Z. and A.R.O. contributed equally to this work.

[2]To whom correspondence may be addressed. Email: klinman@berkeley.edu.

This article contains supporting information online at https://www.pnas.org/lookup/suppl/doi:10.1073/pnas.2211630120/-/DCSupplemental.

Published March 3, 2023.

reorganization terms from the inherently temperature-independent probability of wave function overlap refocuses structure–function–dynamics studies on the protein scaffold itself and allows its deconvolution from the primary chemical bond cleavage event. In this context, SLO was subjected to a combined analysis of the time-, temperature-, and mutation-dependent properties of hydrogen–deuterium exchange as analyzed by mass spectrometry (5). This integrated TDHDX–MS approach aided in the identification of a small subset of SLO-derived peptides for which mutation-induced changes in the activation energies of hydrogen exchange, $E_a(k_{HDX})$, are seen to correlate with changes in the activation energy for the first-order rate constant of catalysis, $E_a(k_{cat})$. The most compelling peptide, 317–334, is located in a solvent-exposed loop (Fig. 1*B*) remote from the sites of mutation.

The nature of the dynamical motions in this loop was further examined through temperature-dependent, time-resolved Stokes shifts measurements that exploited a fluorescent probe incorporated through thiol modification at either position 322 at the tip of the identified thermal network or at a control position 596 (30). The striking observation of an exact correspondence between the E_a for a millisecond catalytic step and for a nanosecond Stokes shift decay process suggested a direct coupling of distal protein motions surrounding the appended probe to active site motions controlling catalysis in the wild-type (WT) enzyme. Herein, we extend these preliminary studies of nanosecond fluorescence Stokes shifts to eight variants of SLO, observing a remarkable identity of the energies of activation for the Stokes shifts decay rates and the millisecond C–H bond cleavage among side chain mutants that are restricted to the identified thermal network. The implication of a site-selective thermal pathway, originating at a solvent-exposed loop and extending toward the buried iron cofactor and substrate-binding site (5, 30), provides a unique opportunity to explore the structural and dynamical features that control C–H activation in enzyme catalysis.

Results

Catalytically Linked Thermal Network in SLO Extends beyond the Initial TDHDX–MS–Defined Pathway. The originally defined thermal pathway for SLO (Fig. 1*B*) was based on the impact of two protein side chains (Leu546 and Ile553 in close proximity to the $Fe^{(III)}$(OH) cofactor and bound linoleic acid substrate) on the TDHDX behavior of a surface loop 20 to 30 Å away (5). Inspection of Fig. 1*B* shows an intermediate region comprising the aliphatic residues Ile552 and Val750 that are positioned to act as mediators between Leu546 and Ile553 and the residues Ser749 and Tyr317 that extend to the surface loop. Of particular interest, neither Ile552 nor Val750 is in direct contact with the reactive carbon, raising the question of their importance and impact to catalytic proficiency. To address this issue, we examined the effect of alanine substitution at Ile552 and Val750, obtaining a suite of kinetic parameters (Table 1). While the magnitude of the difference in the energy of activation for the reaction with H- vs. D-labeled LA substrate [$\Delta E_a = E_a(D) - E_a(H)$] is reduced for V750A, its value is within the experimental error of WT, and the value of ΔE_a for I552A is unchanged. An increase in ΔE_a has been shown to map to a loss of precision in the local positioning of the reactive carbon (C11 of the LA substrate) for SLO (31), as well as for a wide range of H-transfer enzymes (32). In accordance with this behavior, evolutionary selection was recently applied to a primitive form of dihydrofolate reductase (DHFR) showing a progressive decrease in ΔE_a as the evolved enzyme approached the activity of native DHFRs (33). From this study of I552A and V750A, we conclude that ΔE_a is largely unaffected, with the impact of such mutations appearing primarily as a reduction in the

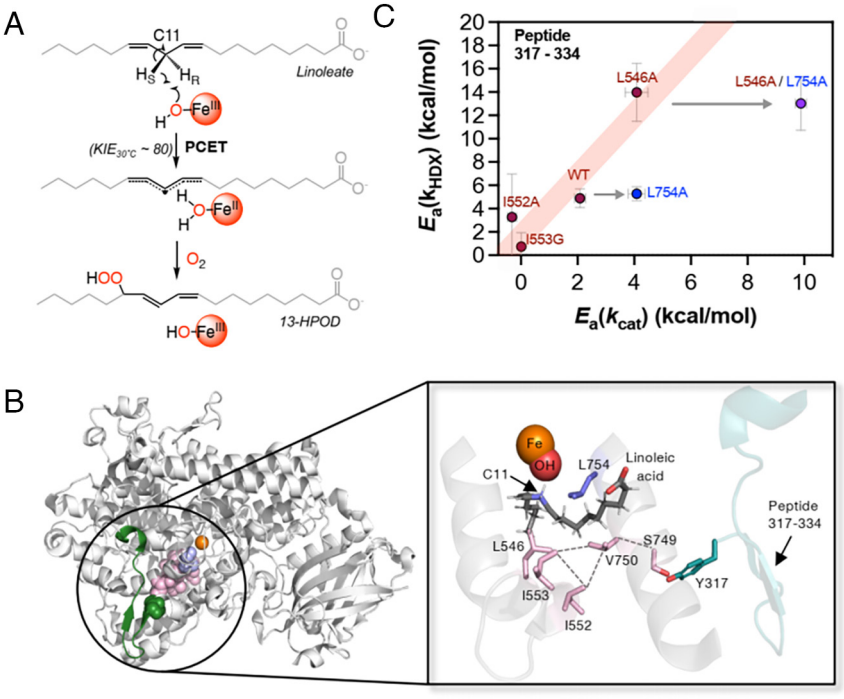

Fig. 1. (*A*) Rate-limiting hydrogen transfer reaction from linoleic acid (LA) catalyzed by an Fe^{III}(OH) cofactor in SLO to form product, 13-HPOD (17). (*B*) X-ray structure of SLO (PDB: 3PZW) depicting the active site Fe (orange), and the network of residues (pink) and thermally activated surface loop (residues 317 to 334, in dark blue-green) inferred from previous TDHDX–MS experiments (5). *Inset*: The bound linoleic acid substrate (dark gray) is modeled from previous calculations (25) and overlaid in this structure. Leu754, which is outside the identified network, is shown in purple. The peptide 317–334 is labeled in blue-green. (*C*) Temperature-dependent HDX–MS analysis. Relationship between the HDX enthalpic barrier (E_a for k_{HDX}) at peptide 317–334 and the enthalpic barrier for hydrogen tunneling (E_a for k_{cat}). New data for I552A are shown and compared with data for other mutants from ref. (34).

Table 1. Comparative kinetic parameters for Ala variants at positions 552 and 750 within the thermal network of SLO*

SLO variant	k_{cat}, s^{-1}	$^{D}k_{cat}$	E_a, kcal/mol	ΔE_a, kcal/mol	Reference
WT	297 (10)	81 (5)	2.1 (0.2)	0.9 (0.2)	Ref. 20
I552A	81 (2)†	60 (2)†	−0.3 (0.2)	1.2 (0.5)	This work*
V750A	218 (8)†	69 (4)†	1.0 (0.4)	0.3 (0.4)	This work*

*Temperature-dependent kinetics data had been reported (35) but were not previously analyzed for E_a and ΔE_a. The full range of additional mutants formerly characterized in this fashion is summarized in *SI Appendix*, Table S1.
†For comparison under similar protein and substrate purification procedures (5), data for WT were recollected using the enzyme preparation of the present study, generating k_{cat} = 359 (7) s^{-1}, $^{D}k_{cat}$ = 57 (2), E_a = 2.4 (0.2) kcal/mol, and ΔE_a = 1.1 (0.1) kcal/mol. Data for k_{cat} and $^{D}k_{cat}$ from this work were collected at 303 K.

enthalpy of activation [E_a(H)] that is accompanied by a reduction in the first-order rate constant (k_{cat}) at 30 °C. The changes in E_a(H) suggest a perturbation (loosening) of structure away from the configuration that is optimal for catalytic turnover in WT, with the impact of I552A exceeding that of V750A.

With the goal of more fully understanding the contribution of residues Ile552 and Val750 to the thermal pathway in SLO, additional independent experimental directions were pursued. First, TDHDX–MS was extended to I552A, which has a more dramatic impact on the catalytic E_a than V750A. Such analysis of I552A results in the same set of nonoverlapping peptides as obtained for WT and other variants (5, 34) (*SI Appendix*, Fig. S1). The majority of the I552A-derived peptides display nearly identical exchange behavior to WT across the five temperatures (10, 20, 25, 30, and 40 °C) analyzed (Dataset S1). The peptide of particular interest is 317–334 that defines a surface loop that was previously shown (5) to undergo strongly correlated alterations in the activation energy for HDX $E_a(k_{HDX})$ and $E_a(k_{cat})$ when interrogating the variants I553G and L546A in relation to WT. Mutation-induced changes to the term $E_a(k_{HDX})$ have been shown to reflect changes in local structural flexibility of a protein. An increase in $E_a(k_{HDX})$ for a particular peptide is attributed to a more rigid and temperature-sensitive structural element, whereas a reduced $E_a(k_{HDX})$ corresponds to a more flexible region (5). The new data for I552A indicate an $E_a(k_{HDX})$ = 3.2(3.7) kcal/mol for peptide 317–334 within experimental error of zero and is analogous to its $E_a(k_{cat})$ = −0.3(0.2) kcal/mol (*SI Appendix*, Table S2). As shown in Fig. 1*C* (red bar), these data for I552A fall on the original correlation of $E_a(k_{HDX})$ and $E_a(k_{cat})$ in support of the inclusion of Ile552 within the defined thermal pathway. We note that mutations at Leu754 (L754A and the double-mutant L546A/L754A) fall off the line correlating $E_a(k_{HDX})$ to $E_a(k_{cat})$ (35), indicating that Leu754 resides outside of the thermal network (Fig. 1*C*); this feature will be discussed further below, serving as a control for time- and temperature-dependent Stokes shift decay analyses. We also observed an unusually large perturbation from I552A on the TDHDX–MS of peptides 541–554 and 555–565 residing near the inferred substrate portal, with peptide 541–554 of I552A indicating a decrease in $E_a(k_{HDX})$ from 23.7(2.0) kcal/mol for WT to 5.64(0.5) kcal/mol (*SI Appendix*, Fig. S2); these data are consistent with an earlier report of an increase in k_{off} values for substrate release in I552A, attributed to a loosening of the substrate portal that is adjacent to the active site (35).

Structural confirmation of the involvement of Ile552 and Val 750 in the thermal network in SLO was pursued through room temperature (RT, 277 to 300 K) X-ray studies. The multiconformer models obtained from qFit (36) uncover coupled, local anisotropic protein dynamical information that is supported by NMR measurements and reflects multiscale motions of the protein backbone and side chains (37). Such studies have been shown to be sensitive to weakly populated substates within a protein conformational ensemble that can be associated with function through comparison of structures for WT enzyme to site-specific mutants (38). Inspection of the electron densities for the RT X-ray structure of WT SLO had indicated a number of alternate side chain conformers at positions Leu546, Ile553, Ile552, and Val750 (5). We have now compared the available RT X-ray data (300 K) for I553G (5) and L546A (34) to WT finding that the I553G variant decreases the conformational space accessed by its proximal Leu546 side chain, while the L546A mutation leaves Ile553 unperturbed and decreases the electron density of an alternate conformer for a second proximal residue Ile552 (*SI Appendix*, Fig. S3). With these observations, we proceeded to examine the impact of both I552A and V750A mutations on nearby residues via RT X-ray structural analysis. While it is possible that changes in side chain conformations and/or populations following site-specific mutagenesis may radiate throughout the protein (38, 39), the impacts of I552A and V750A are found to be concentrated within a region that neighbors the TDHDX–MS–detected thermal pathway (Fig. 2*A*). A dramatic effect of both mutations appears at Leu546, with the loss of one of the two possible side chain conformations of WT (column 1, Fig. 2*A*). The I552A and V750A mutations also produce reciprocal changes to side chain occupancies and/or orientations in Val750 and Ile552, respectively (columns 2 and 3, Fig. 2*A*). Furthermore, mutations at Ile552

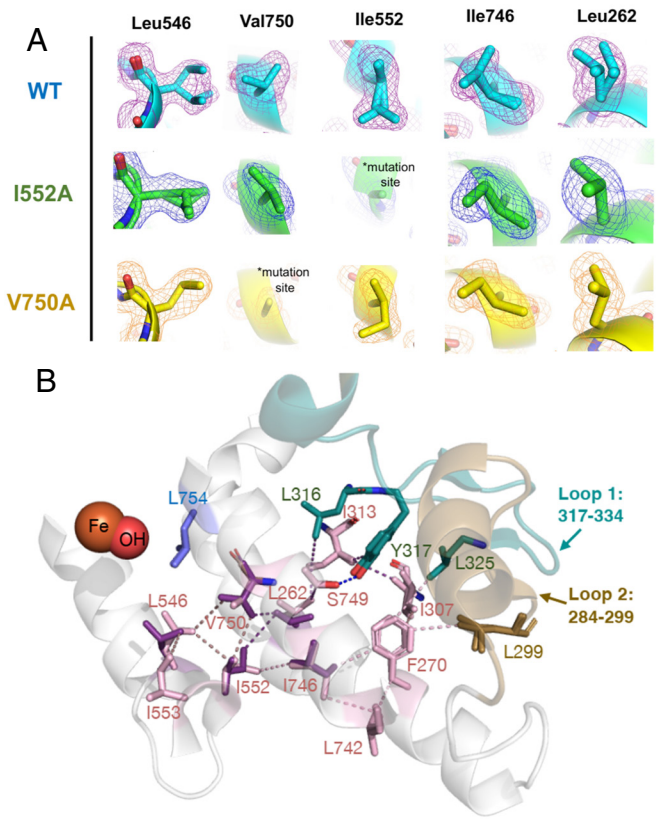

Fig. 2. Room temperature X-ray structure analysis. (*A*) Impact of I552A and V750A mutations on the 300 K X-ray structure electron densities of their respective side chains and those of Leu546, Ile746, and Leu262. (*B*) Connectivity of residues from the Fe active site to the surface loops [loop 1: 317 to 334 (blue-green) and loop 2: 284 to 299 (brown)] in the 300 K X-ray structure of WT SLO (PDB: 5T5V). Multiple side chain conformers detected along the thermal network are purple, with remaining residues colored pink.

and Val750 impact electron densities at side chains Ile746 and Leu262 (columns 4 and 5, Fig. 2*A*); as illustrated, the impact on Ile746 appears greater for nearby I552A than V750A, while Leu262 appears to be altered more from the nearby V750A.

The above analyses provide strong support for the role of both Ile552 and Val750 as mediators between the active site side chains of SLO that are in position to contact bound substrate and an extended thermal network that terminates at the protein–water interface. As a guide for visualizing the entire network, side chain interactions have been traced from Leu546 to the surface loops comprised primarily by the region of protein represented by amino acids 317 to 334 and to a lesser extent the region 284–299, a second peptide shown to undergo correlated motions in the E_a for HDX–MS and catalysis (5) (Fig. 2*B*). Using a cutoff of 4 Å for van der Waals interactions between adjacent side chains, an extended network of amino acids is detected beyond the TDHDX–MS–derived pathway. In particular, Ile552 is seen to act as a core residue, exhibiting steric interactions with Leu546, Val750, and Ile746. Moving further away from these side chains, a number of hydrophobic residues within van der Waals distance (e.g., Leu742, Phe270, Leu299, Ile307, Leu325, and the H-bonding pair Tyr317 and Ser749) can be traced. We note that increasing electron density disorder for such residues closer to the exterior solvent precluded accurate determinations of alternate RT X-ray–derived side chain conformations. As shown in Fig. 2*B*, a cone-shaped region of protein containing activity-related alternate conformers connects the active site to the solvent-exposed loops.

Dynamical Measurements of the Identified Thermal Network in SLO. Stokes shift measurements of SLO were pursued using a wide range of enzyme variants with distinctive trends in $E_a(k_{cat})$ and $E_a(k_{HDX})$. The dye 6-bromoacetyl-2-dimethylaminonaphthalene (BADAN, BD) was appended to position 322 and used as a sensor to probe changes in local solvation dynamics following photoexcitation (40). The main mechanism for fluorescence modulation is through interactions of the surrounding solvent with the electronically excited state of the probe (41), which in the case of BADAN involves changes in polarization of its N,N-dimethylamino- and carbonyl substituents. Nearby Trp residues in proteins have been shown to quench BADAN fluorescence via electron transfer (42). In Q322C-BD SLO, the nearest Trp residue, Trp340, to the BADAN probe at position 322 is 30 to 40 Å away. Molecular dynamics simulations of Q322C-BD show that this distance does not change significantly (*SI Appendix,* Fig. S4), making artifactual quenching of the BADAN probe at the 322 position an unlikely complication.

Four of the protein variants chosen for the current study are in contact either with bound substrate or with each other: I553G, I553A, L546A, and I552A (Fig. 3*A*). Substitution of residues at positions 553 and 546 in the substrate-binding pocket leads to perturbations that increase the $E_a(k_{cat})$ (L546A), decrease the $E_a(k_{cat})$ (I553G), or retain the same $E_a(k_{cat})$ (I553A) as WT (20, 43) (*SI Appendix,* Table S1). Ile552, which is located proximal to Leu546 but is not in direct contact with substrate, produces a decreased $E_a(k_{cat})$ relative to WT (Table 1). The properties of L754A variant make this a valuable internal control. While Leu754 is positioned on an opposite face of the reactive carbon of substrate from Leu546 and L754A produces an elevated enthalpic barrier for catalysis, TDHDX–MS measurements (34) indicate little or no change on $E_a(k_{HDX})$ relative to WT at peptide 317–334 (or other peptides) (Fig. 1*C*). The impacts of L754A on rate and catalytic activation energy have been attributed to an expanded active site that incorporates additional water molecules, thereby altering the active site microenvironment and Fe active site geometry (34). Stokes shift controls involving double mutations with L754A as the parent were also interrogated, involving I553A/L754A and L546A/L754A that exhibit some of the largest observed increases in activation enthalpy for catalysis relative to WT (44) (*SI Appendix,* Table S1). The full set of eight SLO variants display $E_a(k_{cat})$ values from *ca.* 0 to 10 kcal/mol, providing a broad range of catalytic properties (*SI Appendix,* Table S1) from which to

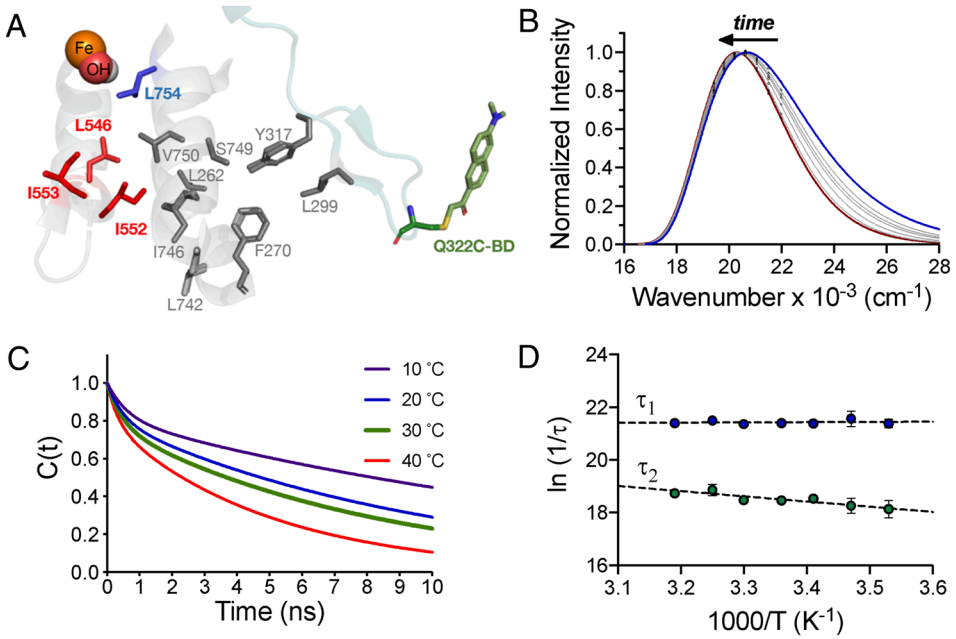

Fig. 3. Temperature-dependent nanosecond fluorescence Stokes shift analysis of a fluorescent probe on the identified surface loop in SLO. (*A*) Location of the mutated active site residues Ile553, Leu546, Ile552 (red), and Leu754 (blue) in relation to the thermally activated loop (317 to 334, blue-green) and the BADAN-labeled Q322C residue (green). The BADAN orientation is based on the optimized structure from ref. 30. (*B*) Representative time-resolved emission spectra (TRES) at 30 °C, pH 9.0, for the L546A SLO mutant. (*C*) Representative time and temperature dependence of the Stokes shift decay rates of L546A. (*D*) Arrhenius plots for the nanosecond Stokes shift decays ($1/\tau_1$, $1/\tau_2$) of L546A.

test the correspondence between the magnitude of activation energies for Stokes shifts decay rates and for the rates of catalysis.

Each of the above-described variants was mutated at Gln322 to cysteine and reacted with the thiol-reactive alkyl bromide group of BADAN according to protocols established with WT SLO (30) (Fig. 3*A*). The resulting bioconjugates were characterized by electrospray ionization mass spectrometry to confirm 1:1 adduct formation (*SI Appendix,* Table S3). To verify the fidelity of the probe attachment to Q322C, liquid chromatography–tandem mass spectrometry was performed on the pepsin digests of each SLO–BD conjugate (*SI Appendix,* Fig. S5), corroborating sole modification at position 322C, with a mass addition (+211 Da) corresponding to the 6-acetyl-2-dimethylaminonaphthalene group. In all instances, the Cys mutation and attachment of BADAN at the Gln322 position yield proteins with almost identical kinetic parameters (k_{cat} and E_a) to the parent SLO (*SI Appendix,* Table S4), making these constructs well suited for probing protein dynamics.

Time-resolved emission spectra (TRES) were constructed from the steady state (*SI Appendix,* Fig. S6) and time-resolved fluorescence decay data (*SI Appendix,* Table S5) upon excitation of BADAN at 373 nm (see *Materials and Methods*). The time-dependent Stokes shift is attributed to solvent/environmental reorganization around the excited state probe and is manifest as continuous red shifts in emission spectra until the steady-state emission wavelength is approximated (45–47). The TRES for the Q322C-BD–labeled SLO mutants at 30 °C are shown in *SI Appendix,* Fig. S7, with total Stokes shifts varying from ~ 700 to 1,800 cm^{-1} (*SI Appendix,* Table S6). The Stokes shift decay curves (*SI Appendix,* Fig. S8) were fit to a biexponential function, indicating a fast (τ_1 ~ 0.5 ns, *ca.* 60%) and a slower (τ_2 ~ 5 to 8 ns, *ca.* 40%) component (*SI Appendix,* Table S6). This bimodal behavior has been shown to be nearly universal and is typically referred to as the bimodality of the reorientational response of biological water (48). The shorter lifetime (τ_1) is typically assigned to the unconstrained (free) water in the biological water layer, and τ_2 is ascribed to the nanosecond reorganization of protein associated with constrained (bound) water (48). Nanosecond Stokes shift decay experiments have been reported for a number of other enzyme systems that include the analysis of a fluorescent probe attached to the surface of a protein tunnel in haloalkane dehalogenase (49) and to the active site of glutaminyl-tRNA synthetase (50). Molecular dynamics simulations support the view that water molecules hydrating the protein surface will undergo restricted translational and rotational motions (51, 52).

Arrhenius plots of the Stokes shift decay rates in SLO variants (*SI Appendix,* Fig. S9 and Table S7) reveal distinctive temperature dependences in the slower component (τ_2) but not in the fast component (τ_1) (Fig. 4 and *SI Appendix,* Fig. S10). In WT SLO, both τ_1 and τ_2 were seen to be temperature dependent (30); however, temperature-independent values for τ_1 appear to be the more general case. The previously reported viscosity independence of k_{cat} in SLO (44, 53) is consistent with a primary role for the hydration shell (related to τ_2) rather than the bulk solvent (related to τ_1) in the enzymatic activation barrier (54). The activation energies (E_a) for τ_2 in SLO range from ~ 0 to 4 kcal/mol (*SI Appendix,* Table S7) and are similar to reported E_a values for the nanosecond dynamics of a solvent-exposed tryptophan in a thermophilic alcohol dehydrogenase (ADH) (55, 56) and the picosecond hydration dynamics around solvent-exposed tryptophan in Dpo4 (57), ApoMb (58), and SNase (59). The comparison of the experimental activation energies for Stokes shift decay rates ($1/\tau_2$) and for k_{cat} as a function of site-specific mutagenesis is presented in Fig. 4. The data indicate a remarkable 1:1 correspondence for WT SLO and four variants within the thermally activated network, I553G, I552A, I553A, and L546A (Fig. 4, red bar), generating a slope of 1.0 (0.1), r^2 = 0.99.

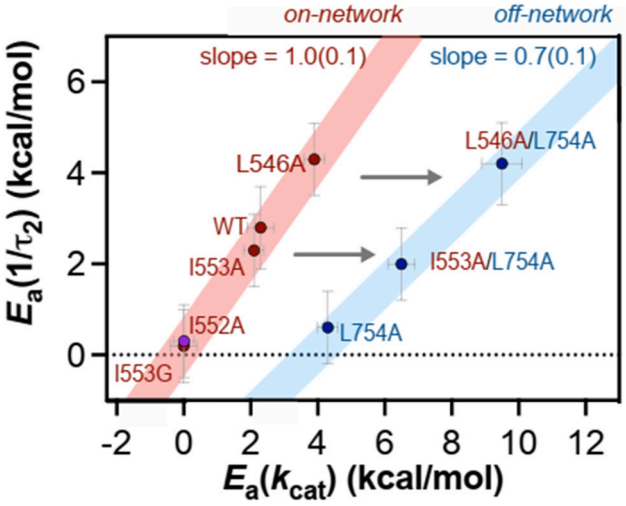

Fig. 4. Comparative activation energies for the Stokes shift decay rates $1/\tau_2$ [$E_a(1/\tau_2)$] and for catalysis [$E_a(k_{cat})$]. The red bar indicates residues that are along the thermal network. Given the very close overlap between the data points for I552A and I553G, the data point for I552A is shown in purple to allow distinction from I553G. The blue bar represents the single-mutant L754A together with two double mutants, I553A/L754A and L546A/L754A. In this case, the temperature dependence of the observed Stokes shift decays arises solely from the on-network mutations (I553A or L546A, labeled red).

Differential scanning calorimetry was pursued to rule out any untoward impact of changes in hydrophobic side chain volume on protein stability in the case of the on-network variants represented in Fig. 4. As summarized in *SI Appendix* (*SI Appendix,* Table S8 and Fig. S11), an analysis of protein unfolding thermodynamics ($\Delta H°$) for mutants relative to native enzyme [$\Delta\Delta H° = \Delta H°$ (mutant) – $\Delta H°$ (WT)] yielded values for $\Delta\Delta H°$ that are within experimental error of each other and in the range of values found for hydrophobic mutations in the prototypic and much smaller enzyme lysozyme (60–62). A second important control is the variant L754A that is concluded to lie outside of the designated SLO thermal network (Fig. 1*C*) (34). The comparative temperature dependencies from Stokes shifts and k_{cat} analyses with L754A are seen to be displaced to the right in Fig. 4 (blue bar). Note that for the double mutants that contain both on-network and off-network mutations, I553A/L754A and L546A/L754A, the temperature dependence of the Stokes shift decay arises solely from the on-network mutation (I553A and L546A). With three data points, this second line of L754A-containing variants displays a slope of 0.7 (0.1) and a correlation coefficient of r^2 = 0.99. The results with L754A mutation indicate that the equivalence of E_a values for catalysis and Stokes shift decay is restricted to residues that have been assigned to the thermal network.

Discussion

These studies extend earlier applications of a range of biophysical tools to the study of SLO that include RT X-ray crystallography, TDHDX, and the temperature dependence of Stokes shift decay (5, 30, 34). Both RT X-ray (38, 63) and TDHDX–MS (4–8) studies provide time-averaged measurements of either amino acid side chain disorder at a single temperature (RT X-ray) or the temperature dependence of local protein unfolding (TDHDX) and share an ability to uncover regions of protein that undergo dynamical changes subsequent to the insertion of

function-altering site-specific mutations. In the present study, we compared RT X-ray structures for WT SLO to single-site mutants with demonstrated impacts on the properties of hydrogen tunneling from C11 of the linoleic acid substrate to the active site Fe^{III}(OH) cofactor (5, 34) (Fig. 1*A*). Electron density analyses (*SI Appendix,* Fig. S3 and Fig. 2*A*) extend the thermal transfer pathway initially identified by TDHDX–MS (5) to an island of primarily hydrophobic side chains that reach from the protein–solvent interface to the active site (Fig. 2*B*). The abundance of hydrophobic residues in this extended network led us to consider other possible clustering of hydrophobic residues in SLO. It has been proposed that the side chains of Ile, Leu, and Val often form hydrophobic clusters (64, 65) which serve as cores of stability and prevent intrusion of water molecules. The hydrophobic clusters in SLO (*SI Appendix,* Fig. S12) were computed using a contacts of structural units algorithm (66). Of considerable interest for how thermal networks may be constructed, the largest calculated hydrophobic cluster in SLO comprises 32 residues and includes the active site residues that are in contact with the linoleic acid substrate (Ile553, Leu546, and Leu754), all of the residues that are experimentally assigned to a thermal activation pathway, and the Ile839 ligand to the Fe center (see below).

In the case of TDHDX–MS, the linear relationship between $E_a(k_{HDX})$and $E_a(k_{cat})$ (34) (Fig. 1*C*, red bar) provided initial insights into the location and composition of a thermal network for enzyme catalysis in SLO. An important caveat of the TDHDX–MS–derived correlation is the significant difference in the magnitudes of $E_a(k_{HDX})$in relation to $E_a(k_{cat})$, as expected for inherently different processes that reflect local and fully reversible protein unfolding events [$E_a(k_{HDX})$] vs. the tuning of active site electrostatics and distances that promote hydrogenic wave function overlap between the donor and acceptor atoms [$E_a(k_{cat})$]. The presented time-dependent Stokes shift analyses (Fig. 4) differ in a fundamental way from the TDHDX–MS experiments, uncovering activation energies for a photo-induced environmental reorganization around a surface-attached probe in SLO that are identical to the measured activation energies for cleavage of the C–H bond of substrate. A limited number of previous studies have shown corresponding enthalpies for distinct kinetic processes within a single system that include a comparison of Stokes shifts and fluorescence anisotropy using the method of tryptophan scanning in DNA polymerase IV (57) and a comparison of the rate of solvent dielectric relaxation to changes in Mössbauer spectra following the photoexcitation of the carbon monoxide–heme complex in myoglobin (54). However, neither of these studies was able to address the physical origins and site specificity of heat activation in the context of an enzyme-catalyzed bond cleavage reaction. The observation of the same enthalpy of activation among variants of SLO for two distinctive chemical processes that take place with rate constants that differ by 10^6-fold provides compelling evidence for rapid (faster than nanosecond), temperature-dependent protein restructuring that connects the thermal energy of the solvent bath with the remote bond cleavage step in SLO over an average distance of *ca.* 20 to 30 Å. The regional specificity of this heat flow, as revealed from in-depth studies of TDHDX–MS and RT X-ray, illustrates the importance of anisotropic thermal conduits that are able to generate activated enzyme–substrate complexes while minimizing indiscriminate interference from nonproductive protein motions that could slow down or eliminate catalysis.

There has been a recent resurgence and growing interest in understanding and harnessing the role of quantum mechanics, including spin coherence, entanglement, and tunneling, in biological and other macroscopic processes (67, 68). Among the unresolved questions is our ability to determine and quantify the link, and possible synergy, between classical and quantum behavior and the degree to which thermal "noise" at the warm temperatures of biology influences the efficiency of quantum effects. We note that an earlier computational analysis of promoting vibrations in lactate dehydrogenase had led to the proposal of a preferred channel for energy transfer (69). A defining feature from studies of SLO is the primacy of the extended protein scaffold in overcoming the energetic barriers of tunneling; this necessitates a simultaneous reduction in the donor–acceptor distance (DAD) and the creation of transient degeneracy between reactant and product states (22, 23).

The spatial and temporal resolution of functionally impactful protein motions in SLO provided by the present study leads us to propose an atomistic mechanism for how classical motions within the protein scaffold of SLO enable quantum tunneling: As a frame of reference, the substrate linoleic acid is modeled into the available X-ray structure for SLO (25). The fluctuations in the identified localized region of aliphatic residues, Fig. 5*A*, are influenced by the remote, solvent-exposed loops and culminate at Leu546, the key residue in direct contact with the reactive carbon of substrate (C11). Thermally activated changes in side chain positions within this region are positioned to moderate the distance between the substrate hydrogen donor and its acceptor, the iron-bound hydroxide ion, leading to a transient reduction in DAD from an initial van der Waals interaction (Fig. 5*B* and ref. 31) to a tunneling-ready distance of *ca.* 2.7 Å (22, 23, 70). Thermally activated motions that alter the substrate cofactor distance may reasonably be expected to also propagate along the substrate chain, producing a concomitant reduction in distance between a remote hydrophobic carbon of substrate (position C14 in the presented orientation) and Ile839. The residue Ile839 is directly ligated to the active site iron of SLO and has been predicted to tune the electrostatic properties of quantum tunneling by moderating hydrogen-bonding interactions between the iron-bound hydroxide ion and its C-terminal carboxylate (24, 71). Accordingly, a shared protein "quake" is proposed to simultaneously reduce the H–donor–acceptor distance to tunneling appropriate distances and to produce the matched reactant/product energy states that are a prerequisite for hydrogenic wave function overlap.

A central feature of the presented data is the observation that two distinct physical processes, fluorescence Stokes shift decays (nanoseconds) and substrate turnover (milliseconds), share a common activation energy (E_a) while differing in rate by 10^6-fold. In the case of the tunneling-based C–H cleavage reaction of SLO, developed analytical rate expressions are capable of reproducing both the size and temperature dependence of isotope effects on the tunneling rate, $k_{(tun)}$, but not the magnitude of the observed rate of catalysis, k_{obs} (72). This has been attributed to the essential role of conformational ensembles, where only a small fraction of enzyme undergoes reaction at any time according to Eqs. **1** and **2** as follows:

$$k_{obs} = F_{(conf)} \times k_{(tun)}, \quad [1]$$

$$F_{(conf)} = \frac{E_{(active)}}{E_{(total)}}. \quad [2]$$

Equating P_{conf} to $F_{(conf)}$, a comprehensive formulation for the observation of different rate constants that arise from a shared thermal activation of the protein scaffold can be written, Eq.3, as follows:

$$k_{obs} = P_{conf} \bullet k_{intrinsic}. \quad [3]$$

As represented, the measured rate constant k_{obs} depends on both the rate of the temperature-dependent activation of the specific

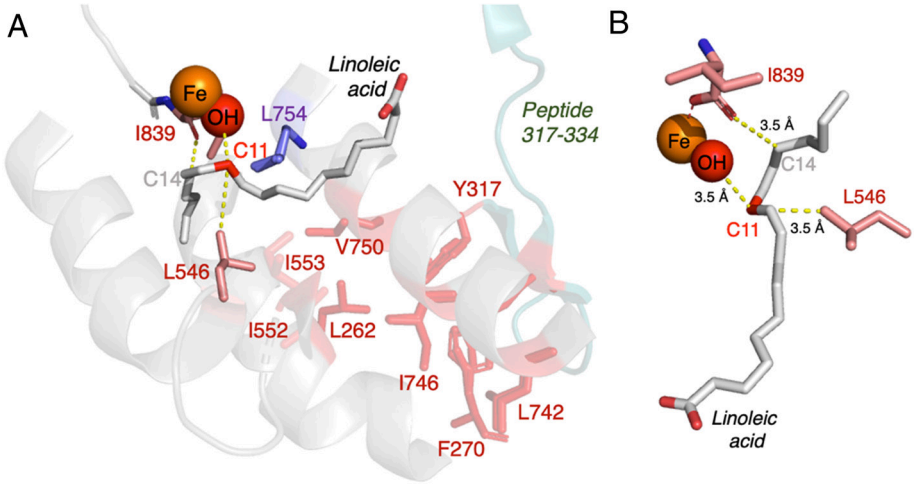

Fig. 5. Graphical representation of the proposed role of thermally activated protein scaffold motions in modulating the donor–acceptor distance (DAD) and reactant/product energetics in SLO-catalyzed hydrogen tunneling. (*A*) The bound linoleic acid substrate (gray) is modeled from previous quantum mechanics/molecular mechanics calculations (25) and overlaid in the WT RT X-ray structure (PDB: 5T5V). The experimentally identified solvent-exposed loop (peptide 317–334) is shown in blue-green. Connecting this loop to the active site is a network of mainly aliphatic residues (in red) that mediates the heat transfer and culminates at Leu546 in van der Waals contact with the reactive carbon C11. (*B*) Interactions between LA and the Fe(OH) cofactor are dependent on fluctuations of Leu546 and Ile839 that arise from within the defined thermal network. The side chain Leu546 influences the positioning of the carbon backbone of bound LA, while Ile839 mediates the electrostatic environment.

protein thermal network, contained within $k_{intrinsic}$, and P_{conf}, the probability that the resulting structural activation is sufficient for the process undergoing measurement. In the case of a fully optimized enzyme-catalyzed reaction, P_{conf} will be very small, a result of the dependence of productive barrier crossings on a multitude of transiently optimized electrostatic interactions and precise internuclear distances. The magnitude of P_{conf} can reasonably be expected to become much larger in the case of the Stokes shifts behavior of a surface-appended fluorophore, given the availability of a wide range of both protein and solvent interactions for the stabilization of excited state dipoles, as reflected in the observation of Stokes shifts within the picosecond to nanosecond regimes (30, 55–58). This feature is attributed to the origin of the 10^6-fold increase in k_{obs} for Stokes shifts with the BADAN-labeled SLO that occur with E_a values identical to enzymatic turnover. Although quantitative measurements of the contributions of $\Delta H^{\ddagger}$ and $\Delta S^{\ddagger}$ to the free energy of activation of enzymatic reactions are readily available in the literature, structural and dynamical interpretation of these parameters has been lacking. In the context of the model developed herein for the SLO reaction, the value of $\Delta H^{\ddagger}$ is seen to derive entirely from the thermal activation of the identified protein network (Fig. 5*A*), with $\Delta S^{\ddagger}$ reflecting the frequency with which transiently excited protein states are congruent with productive H tunneling.

Extensive literature discussions of the role of protein dynamics in enzyme catalysis have been primarily focused on the importance of distributed conformational protein substates that are readily accessible and rapidly interconverting near room temperature (73–77). The presented work raises the question of the relationship of such conformational landscapes to the participation of anisotropic networks that provide explicit pathways for productive heat transfer in thermally activated enzyme reactions. Our multitiered working model of protein dynamics integrates the growing body of experimental evidence for protein-embedded thermal networks (4–8) that enable rapid, long-distance initiation of active site chemistry: First, according to the principle of conformational selection (Fig. 6), as conceptualized by Frauenfelder for ligand-binding dynamics in myoglobin (78) and developed by Kern and coworkers for catalyzed reactions (75, 76), substrate binding leads to shifts in the conformational ensemble of apoenzyme toward configurations that place the reactive components of an enzyme active site in proximity to regions of protein capable of efficient heat transmission from solvent to the active site (Fig. 6*A*). Subsequent sampling of multiple conformational substates within the enzyme-substrate (ES) complex is expected to refine the precision of interactions of bound substrate with the embedded thermal network (Fig. 6*B*) (conversion of ES to ES′). Barrier crossings arise from a combination of optimized ES′ states in relation to the site-specific, long-range thermal activation pathway. The overall properties of Fig. 6 provide a context from which to rationalize the large and growing body of evidence from directed evolution (79–82) and high-throughput screening (83) that discrete regions distal to the active site play essential roles in enzyme catalysis (84).

An earlier study of a thermophilic alcohol dehydrogenase (ht-ADH) had been designed to compare intrinsic protein (tryptophan) fluorescence to the catalyzed reaction. Using protein constructs in which single-site tryptophan side chains were installed either at the active site or in a remote-embedded position, a one-to-one correspondence between the activation energies for nanosecond fluorescence lifetimes and/or Stokes shifts and the millisecond rate of hydride transfer from substrate to the nicotinamide adenine dinucleotide cofactor was restricted to the Trp residing behind bound substrate (55, 56). In a separate analysis of Förster resonance energy transfer (FRET) kinetics between a second interior Trp residue and the nicotinamide ring of bound cofactor, identical enthalpies of activation were also observed for microsecond FRET and millisecond catalysis (85). This correspondence of activation energies for protein structural rearrangements and C–H activation on different timescales is similar to SLO. However, ht-ADH differs greatly from SLO regarding the chemical reaction catalyzed, the transfer of hydrogen as a hydride ion rather than as a hydrogen atom, and values for E_a (11 to 15 kcal/mol) that are considerably larger than the magnitude of E_a for WT SLO and variants (2 to 4 kcal/mol). Additionally, studies of SLO involve an appended fluorescent probe that connects the protein surface to the remote active site over a distance of *ca.* 30 Å, raising the question of the mechanism whereby a long-distance, thermally activated rearrangement of the protein scaffold can support both nanosecond fluorescence at the protein surface and remote millisecond catalysis.

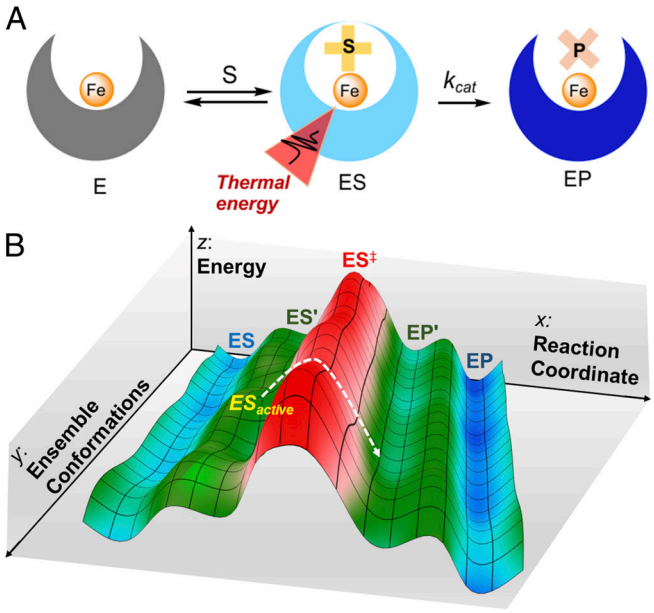

Fig. 6. An integrated model of the multiple tiers of protein dynamics. (*A*) Binding of substrate to enzyme produces changes in both protein structure and flexibility (illustrated using the iron in SLO as a generic frame of reference). The process of conformational selection drives the enzyme from a distribution of substrate-free to substrate-bound conformational substates (75, 76, 78), placing the substrate in proximity to the active site metal and an extended thermal network for productive heat transfer (labeled red cone). (*B*) View of an energy landscape that leads to barrier crossings (adapted from ref. 86). The initially formed enzyme–substrate complex (ES, blue) further samples a wide range of RT-accessible protein conformational substates (ES′, green) (*y* axis, designated ensemble conformations). Only a fraction of ES′ will be optimized with regard to the protein-embedded thermal network (ES_{active}) to achieve efficient barrier crossings (*x* axis, designated reaction coordinate). The very low probability of femtosecond barrier crossings is expected to be a reflection of a small fraction of productive protein substates within the conformational ensemble together with an ongoing partitioning of the network-specific heat transfer between cooperative protein restructuring and dissipation.

Pagano et al. have implicated picosecond oscillations as the origin of the temperature dependence of the kinetic isotope effect in the enzyme formate dehydrogenase (87). In X-ray free electron laser-based studies of heat evolution in a light-activated protein, protein structural changes are found to radiate out from the active site to solvent on a timescale of femtoseconds to picoseconds (88). This range of timescales is consistent with experimental and computational studies of a number of well-studied model systems, e.g., myoglobin and albumin, that consistently indicate lifetimes in the range of 1 to 50 ps for heat flow in proteins over distances of tens of angstroms (89–94). Using a different approach involving site-specific incorporation of a local heater, Baumann et al. were able to detect picosecond vibrational energy transfer within the protein interaction domain of PDZ3 (95). Such data support the view that SLO is able to support long-range (over a distance of 20 to 30 Å), picosecond heat transfer from the protein–solvent interface to the active site. The presence of two surface loops at the end of the SLO thermal network (Fig. 2) further suggests that the initial heat transfer to surface loops 1 and 2 may act as a "trigger" for the ensuing rapid, long-range, and temperature-dependent protein restructuring.

We note that none of the presented studies directly address the question of whether rapid, cooperative heat flow through a protein can deviate from a fully equilibrated process. In a recent study of infrared-detected protein motions following photochemical excitation of a surface probe in bovine serum albumin, an out-of-equilibrium protein quake was proposed with properties of a Fröhlich-like condensate that is comprised of coupled low-frequency vibrations (96). In the present study, the entire protein will be in equilibrium with the bulk solvent at each temperature. However, the contribution of anisotropic thermal conduits to protein thermal activation provides a different view of "apparent out-of-equilibrium" behavior in proteins: We propose that the irregular topology of globular proteins provides a means for non-random heat distribution at fixed temperatures, with specific regions more efficient than average with regard to the coupling of protein scaffold motions to reaction barrier crossings.

The presented model for protein dynamics (Fig. 6) is very different from previous textbook descriptions of enzyme catalysis that are primarily focused on static enzyme structures and are rooted in the principle of "enhanced transition state binding" (97, 98). Although this particular study is focused on an enzyme reaction that proceeds via deep hydrogen tunneling, a combination of distributed protein conformational substates and embedded thermal networks within a protein scaffold is likely to play a key physical role in enzymatic rate enhancements independent of the reaction catalyzed (99) The dominant role of the protein scaffold has been visualized through a combination of conformational selection (Fig. 6*A*) and subsequent conformational sampling that occurs subsequent to formation of the ES complex (Fig. 6*B*). As illustrated, the primary coordinate for catalysis lies on the *x*-axis that involves site-specific distribution of heat into the protein scaffold to reach high-energy states capable of barrier crossings ($ES^{‡}$, labeled red); this property is shown as acting in concert with a distributed conformational landscape (*y*-axis, labeled green) that enhances the specificity with which a subset of ES complexes are positioned to respond to local anisotropic heat transfer. This combined involvement of protein-embedded thermal networks with protein conformational selection and sampling that occur in response to binding of substrate (for enzyme catalysis) can be extended to the binding of allosteric effector (in the case of enzyme regulation). The newly presented data and interpretation both emphasize the unique properties of enzyme reactivity relative to the reaction of small molecules in the condensed phase and serve as a launching point to answering the long-sought goal of integrating the protein matrix into our understanding of the origins of naturally evolved enzymatic rate accelerations and our ability to carry over this knowledge into rational de novo design of proteins and other soft materials.

Materials and Methods

General. All reagents were purchased from commercial sources at the highest grade available. Water was purified to a resistivity of 18.2 MΩ cm (at 25 °C) using a Milli-Q Gradient ultrapure water purification system (Millipore). DNA sequencing was performed at the UC Berkeley DNA Sequencing Facility. Mass spectrometric analysis of intact and pepsin-digested proteins was performed at the UC Berkeley QB3/Chemistry Mass Spectrometry Facility. Fluorescence emission spectra of the BADAN-labeled mutants were collected on a custom-built Fluorolog-3 spectrofluorometer (Horiba Jobin-Yvon). Excitation was achieved with a 450-W xenon lamp. The light was focused using a double Czerny–Turner excitation monochromator (1-nm bandpass) with 1,200 grooves/mm blazed at 330 nm. Photons from sample emission were focused using a single Czerny–Turner monochromator (10-nm bandpass) with 1,200 grooves/mm blazed at 500 nm. The excitation and emission optics were calibrated using the lamp spectral maximum at 467 nm and the water Raman scattering band at 397 nm, respectively, using high-pressure liquid chromatography-grade water in a quartz cuvette. Further details regarding *Materials and Methods* are provided in *SI Appendix* available for this paper at https://www.pnas.org/lookup/suppl/doi:10.1073/pnas.2211630120/-/DCSupplemental.

Data, Materials, and Software Availability. Summary tables of all kinetic and thermodynamic parameters and fluorescence and crystallography data measured

for each mutant are also included. The atomic models have been deposited at the Protein Data Bank with PDB IDs 7SOI (I552A SLO) and 7SOJ (V750A SLO). All other data are included in the article and/or *SI Appendix*.

ACKNOWLEDGMENTS. We thank Prof. Tom Spiro and Prof. Nigel Richards for their helpful and stimulating discussions. We also thank the members of the Klinman laboratory for the insightful discussions about the manuscript, specifically Dr. Emily Thompson and Dr. Shuaihua Gao for assistance with programming and data analysis. This research was supported by funding from the NIH grants to J.P.K. (GM118117), A.R.O. [GM113432 (F32)], and A.T.I. (1S10OD020062-01). J.P.T.Z. thanks the University of California President's Postdoctoral Program for a fellowship. Data collection at BL 8.3.1 at the Advanced Light Source was supported by the Director, Office of Science, Office of Basic Energy Sciences, of the US Department of Energy under contract no. DE-AC02-05CH11231, UC Office of the President, Multicampus Research Programs and Initiatives grant MR 15 32859, the Program for Breakthrough Biomedical Research, which was partially funded by the Sandler Foundation, and the NIH P30GM124169.

Author affiliations: [a]California Institute for Quantitative Biosciences, University of California Berkeley, Berkeley, CA 94720; [b]Department of Chemistry, University of California Berkeley, Berkeley, CA 94720; [c]Department of Chemistry, East Carolina University, Greenville, NC 27858; and [d]Department of Molecular and Cell Biology, University of California Berkeley, Berkeley, CA 94720

1. M. H. Vos, F. Rappaport, J.-C. Lambry, J. Breton, J.-L. Martin, Visualization of coherent nuclear motion in a membrane protein by femtosecond spectroscopy. *Nature* **363**, 320–325 (1993).
2. H. Wang *et al.*, Protein dynamics control the kinetics of initial electron transfer in photosynthesis. *Science* **316**, 747 (2007).
3. D. J. Heyes *et al.*, Photochemical mechanism of light-driven fatty acid photodecarboxylase. *ACS Catal.* **10**, 6691–6696 (2020).
4. Z.-X. Liang, T. Lee, K. A. Resing, N. G. Ahn, J. P. Klinman, Thermal-activated protein mobility and its correlation with catalysis in thermophilic alcohol dehydrogenase. *Proc. Natl. Acad. Sci. U.S.A.* **101**, 9556 (2004).
5. A. R. Offenbacher *et al.*, Hydrogen-deuterium exchange of lipoxygenase uncovers a relationship between distal, solvent exposed protein motions and the thermal activation barrier for catalytic proton-coupled electron tunneling. *ACS Cent. Sci.* **3**, 570–579 (2017).
6. J. Zhang, J. L. Balsbaugh, S. Gao, N. G. Ahn, J. P. Klinman, Hydrogen deuterium exchange defines catalytically linked regions of protein flexibility in the catechol O-methyltransferase reaction. *Proc. Natl. Acad. Sci. U.S.A.* **117**, 10797 (2020).
7. S. Gao *et al.*, Hydrogen-deuterium exchange within adenosine deaminase, a TIM barrel hydrolase, identifies networks for thermal activation of catalysis. *J. Am. Chem. Soc.* **142**, 19936–19949 (2020).
8. E. J. Thompson, A. Paul, A. T. Iavarone, J. P. Klinman, Identification of thermal conduits that link the protein-water interface to the active site loop and catalytic base in enolase. *J. Am. Chem. Soc.* **143**, 785–797 (2021).
9. Z. Wang *et al.*, Ultrafast flash thermal conductance of molecular chains. *Science* **317**, 787 (2007).
10. L. Martínez, A. C. M. Figueira, P. Webb, I. Polikarpov, M. S. Skaf, Mapping the intramolecular vibrational energy flow in proteins reveals functionally important residues. *J. Phys. Chem. Lett.* **2**, 2073–2078 (2011).
11. J. Helbing *et al.*, Temperature dependence of the heat diffusivity of proteins. *J. Phys. Chem. A* **116**, 2620–2628 (2012).
12. I. V. Rubtsov, A. L. Burin, Ballistic and diffusive vibrational energy transport in molecules. *J. Chem. Phys.* **150**, 020901 (2019).
13. M. Mizuno, Y. Mizutani, Role of atomic contacts in vibrational energy transfer in myoglobin. *Biophys. Rev.* **12**, 511–518 (2020).
14. H. Poudel, K. M. Reid, T. Yamato, D. M. Leitner, Energy transfer across nonpolar and polar contacts in proteins: Role of contact fluctuations. *J. Phys. Chem. B* **124**, 9852–9861 (2020).
15. L. Valiño Borau, A. Gulzar, G. Stock, Master equation model to predict energy transport pathways in proteins. *J. Chem. Phys.* **152**, 045103 (2020).
16. R. Kozlowski, J. Zhao, R. B. Dyer, Acceleration of catalysis in dihydrofolate reductase by transient, site-specific photothermal excitation. *Proc. Natl. Acad. Sci. U.S.A.* **118**, e2014592118 (2021).
17. M. H. Glickman, J. S. Wiseman, J. P. Klinman, Extremely large isotope effects in the soybean lipoxygenase-linoleic acid reaction. *J. Am. Chem. Soc.* **116**, 793–794 (1994).
18. H. Porta, M. Rocha-Sosa, Plant lipoxygenases. Physiological and molecular features. *Plant Physiol.* **130**, 15 (2002).
19. K. W. Rickert, J. P. Klinman, Nature of hydrogen transfer in soybean lipoxygenase 1: Separation of primary and secondary isotope effects. *Biochemistry* **38**, 12218–12228 (1999).
20. M. J. Knapp, K. Rickert, J. P. Klinman, Temperature-dependent isotope effects in soybean lipoxygenase-1: Correlating hydrogen tunneling with protein dynamics. *J. Am. Chem. Soc.* **124**, 3865–3874 (2002).
21. S. Hu *et al.*, Extremely elevated room-temperature kinetic isotope effects quantify the critical role of barrier width in enzymatic C-H activation. *J. Am. Chem. Soc.* **136**, 8157–8160 (2014).
22. E. Hatcher, A. V. Soudackov, S. Hammes-Schiffer, Proton-coupled electron transfer in soybean lipoxygenase. *J. Am. Chem. Soc.* **126**, 5763–5775 (2004).
23. S. Hammes-Schiffer, Hydrogen tunneling and protein motion in enzyme reactions. *Acc. Chem. Res.* **39**, 93–100 (2006).
24. B. Salna, A. Benabbas, D. Russo, P. M. Champion, Tunneling kinetics and nonadiabatic proton-coupled electron transfer in proteins: The effect of electric fields and anharmonic donor-acceptor interactions. *J. Phys. Chem. B* **121**, 6869–6881 (2017).
25. P. Li, A. V. Soudackov, S. Hammes-Schiffer, Fundamental insights into proton-coupled electron transfer in soybean lipoxygenase from quantum mechanical/molecular mechanical free energy simulations. *J. Am. Chem. Soc.* **140**, 3068–3076 (2018).
26. P. M. Kiefer, J. T. Hynes, Kinetic isotope effects for nonadiabatic proton transfer reactions in a polar environment. 1. Interpretation of tunneling kinetic isotopic effects. *J. Phys. Chem. A* **108**, 11793–11808 (2004).
27. M. J. Knapp, J. P. Klinman, Environmentally coupled hydrogen tunneling. *Eur. J. Biochem.* **269**, 3113–3121 (2002).
28. M. J. Sutcliffe, N. S. Scrutton, A new conceptual framework for enzyme catalysis. *Eur. J. Biochem.* **269**, 3096–3102 (2002).
29. J. P. Klinman, A. R. Offenbacher, S. Hu, Origins of enzyme catalysis: Experimental findings for C-H activation, new models, and their relevance to prevailing theoretical constructs. *J. Am. Chem. Soc.* **139**, 18409–18427 (2017).
30. J. P. T. Zaragoza *et al.*, Detecting and characterizing the kinetic activation of thermal networks in proteins: Thermal transfer from a distal, solvent-exposed loop to the active site in soybean lipoxygenase. *J. Phys. Chem. B* **123**, 8662–8674 (2019).
31. A. R. Offenbacher, A. Sharma, P. E. Doan, J. P. Klinman, B. M. Hoffman, The soybean lipoxygenase-substrate complex: Correlation between the properties of tunneling-ready states and ENDOR-detected structures of ground states. *Biochemistry* **59**, 901–910 (2020).
32. J. P. Klinman, A. R. Offenbacher, Understanding biological hydrogen transfer through the lens of temperature dependent kinetic isotope effects. *Acc. Chem. Res.* **51**, 1966–1974 (2018).
33. P. Singh *et al.*, Evolution of the chemical step in enzyme catalysis. *ACS Catal.* **11**, 6726–6732 (2021).
34. S. Hu, A. R. Offenbacher, E. D. Lu, J. P. Klinman, Comparative kinetic isotope effects on first- and second-order rate constants of soybean lipoxygenase variants uncover a substrate-binding network. *J. Biol. Chem.* **294**, 18069–18076 (2019).
35. S. Hu *et al.*, Biophysical characterization of a disabled double mutant of soybean lipoxygenase: The "undoing" of precise substrate positioning relative to metal cofactor and an identified dynamical network. *J. Am. Chem. Soc.* **141**, 1555–1567 (2019).
36. D. A. Keedy, J. S. Fraser, H. van den Bedem, Exposing hidden alternative backbone conformations in x-ray crystallography using qFit. *PLoS Comput. Biol.* **11**, e1004507 (2015).
37. R. B. Fenwick, H. van den Bedem, J. S. Fraser, P. E. Wright, Integrated description of protein dynamics from room-temperature X-ray crystallography and NMR. *Proc. Natl. Acad. Sci. U.S.A.* **111**, E445 (2014).
38. J. S. Fraser *et al.*, Hidden alternative structures of proline isomerase essential for catalysis. *Nature* **462**, 669–673 (2009).
39. H. van den Bedem, G. Bhabha, K. Yang, P. E. Wright, J. S. Fraser, Automated identification of functional dynamic contact networks from X-ray crystallography. *Nat. Methods* **10**, 896–902 (2013).
40. R. B. Macgregor, G. Weber, Estimation of the polarity of the protein interior by optical spectroscopy. *Nature* **319**, 70 (1986).
41. P. Abbyad *et al.*, Measurement of solvation responses at multiple sites in a globular protein. *J. Phys. Chem. B* **111**, 8269–8276 (2007).
42. P. Pospíšil *et al.*, Fluorescence quenching of (dimethylamino)naphthalene dyes Badan and Prodan by tryptophan in cytochromes P450 and micelles. *J. Phys. Chem. B* **118**, 10085–10091 (2014).
43. M. P. Meyer, D. R. Tomchick, J. P. Klinman, Enzyme structure and dynamics affect hydrogen tunneling: The impact of a remote side chain (I553) in soybean lipoxygenase-1. *Proc. Natl. Acad. Sci. U.S.A.* **105**, 1146 (2008).
44. S. C. Sharma, J. P. Klinman, Kinetic detection of orthogonal protein and chemical coordinates in enzyme catalysis: Double mutants of soybean lipoxygenase. *Biochemistry* **54**, 5447–5456 (2015).
45. M. G. Badea, L. Brand, "[17]Time-resolved fluorescence measurements" in *Methods in Enzymology* (Academic Press, 1979), **vol. 61**, pp. 378–425.
46. J. R. Lakowicz, H. Cherek, G. Laczko, E. Gratton, Time-resolved fluorescence emission spectra of labeled phospholipid vesicles, as observed using multi-frequency phase-modulation fluorometry. *Biochim. Biophys. Acta Biomembr.* **777**, 183–193 (1984).
47. M. L. Horng, J. A. Gardecki, A. Papazyan, M. Maroncelli, Subpicosecond measurements of polar solvation dynamics: Coumarin 153 revisited. *J. Phys. Chem.* **99**, 17311–17337 (1995).
48. N. Nandi, B. Bagchi, Dielectric relaxation of biological water. *J. Phys. Chem. B* **101**, 10954–10961 (1997).
49. A. Jesenská *et al.*, Nanosecond time-dependent Stokes shift at the tunnel mouth of haloalkane dehalogenases. *J. Am. Chem. Soc.* **131**, 494–501 (2009).
50. S. Guha *et al.*, Slow solvation dynamics at the active site of an enzyme: Implications for catalysis. *Biochemistry* **44**, 8940–8947 (2005).
51. V. Makarov, B. M. Pettitt, M. Feig, Solvation and hydration of proteins and nucleic acids: A theoretical view of simulation and experiment. *Acc. Chem. Res.* **35**, 376–384 (2002).
52. S. Pal, S. Bandyopadhyay, Importance of protein conformational motions and electrostatic anchoring sites on the dynamics and hydrogen bond properties of hydration water. *Langmuir* **29**, 1162–1173 (2013).
53. M. H. Glickman, J. P. Klinman, Nature of rate-limiting steps in the soybean lipoxygenase-1 reaction. *Biochemistry* **34**, 14077–14092 (1995).
54. H. Frauenfelder *et al.*, A unified model of protein dynamics. *Proc. Natl. Acad. Sci. U.S.A.* **106**, 5129 (2009).
55. C. W. Meadows, J. E. Tsang, J. P. Klinman, Picosecond-resolved fluorescence studies of substrate and cofactor-binding domain mutants in a thermophilic alcohol dehydrogenase uncover an extended network of communication. *J. Am. Chem. Soc.* **136**, 14821–14833 (2014).
56. C. W. Meadows, R. Ou, J. P. Klinman, Picosecond-resolved fluorescent probes at functionally distinct tryptophans within a thermophilic alcohol dehydrogenase: Relationship of temperature-dependent changes in fluorescence to catalysis. *J. Phys. Chem. B* **118**, 6049–6061 (2014).
57. Y. Qin, L. Wang, D. Zhong, Dynamics and mechanism of ultrafast water–protein interactions. *Proc. Natl. Acad. Sci. U.S.A.* **113**, 8424 (2016).
58. Y. Qin, L. Zhang, L. Wang, D. Zhong, Observation of the global dynamic collectivity of a hydration shell around apomyoglobin. *J. Phys. Chem. Lett.* **8**, 1124–1131 (2017).

59. M. Jia *et al.*, Determination of protein surface hydration by systematic charge mutations. *J. Phys. Chem. Lett.* **6**, 5100–5105 (2015).
60. A. E. Eriksson, W. A. Baase, B. W. Matthews, Similar hydrophobic replacements of Leu99 and Phe153 within the core of T4 lysozyme have different structural and thermodynamic consequences. *J. Mol. Biol.* **229**, 747–769 (1993).
61. A. E. Eriksson *et al.*, Response of a protein structure to cavity-creating mutations and its relation to the hydrophobic effect. *Science* **255**, 178–183 (1992).
62. K. Takano *et al.*, Contribution of hydrophobic residues to the stability of human lysozyme: Calorimetric studies and X-ray structural analysis of the five isoleucine to valine mutants. *J. Mol. Biol.* **254**, 62–76 (1995).
63. J. S. Fraser *et al.*, Accessing protein conformational ensembles using room-temperature X-ray crystallography. *Proc. Natl. Acad. Sci. U.S.A.* **108**, 16247 (2011).
64. S. V. Kathuria, Y. H. Chan, R. P. Nobrega, A. Özen, C. R. Matthews, Clusters of isoleucine, leucine, and valine side chains define cores of stability in high-energy states of globular proteins: Sequence determinants of structure and stability. *Protein Sci.* **25**, 662–675 (2016).
65. S. Basak *et al.*, Networks of electrostatic and hydrophobic interactions modulate the complex folding free energy surface of a designed βα protein. *Proc. Natl. Acad. Sci. U.S.A.* **116**, 6806 (2019).
66. N. Ferruz, S. Schmidt, B. Höcker, ProteinTools: A toolkit to analyze protein structures. *Nucleic Acids Res.* **49**, W559–W566 (2021).
67. Y. Kim *et al.*, Quantum biology: An update and perspective. *Quantum Rep.* **3**, 80–126 (2021).
68. J. Cao *et al.*, Quantum biology revisited. *Sci. Adv.* **6**, eaaz4888 (2020).
69. A. Davarifar, D. Antoniou, S. D. Schwartz, The promoting vibration in human heart lactate dehydrogenase is a preferred vibrational channel. *J. Phys. Chem. B* **115**, 15439–15444 (2011).
70. A. V. Soudackov, S. Hammes-Schiffer, Proton-coupled electron transfer reactions: Analytical rate constants and case study of kinetic isotope effects in lipoxygenase. *Faraday Discuss.* **195**, 171–189 (2016).
71. P. Phatak, I. Sumner, S. S. Iyengar, Gauging the flexibility of the active site in soybean lipoxygenase-1 (SLO-1) through an atom-centered density matrix propagation (ADMP) treatment that facilitates the sampling of rare events. *J. Phys. Chem. B* **116**, 10145–10164 (2012).
72. S. C. Althorpe *et al.*, Non-adiabatic reactions: General discussion. *Faraday Discuss.* **195**, 311–344 (2016).
73. S. C. L. Kamerlin, A. Warshel, At the dawn of the 21st century: Is dynamics the missing link for understanding enzyme catalysis? *Proteins* **78**, 1339–1375 (2010).
74. V. C. Nashine, S. Hammes-Schiffer, S. J. Benkovic, Coupled motions in enzyme catalysis. *Curr. Opin. Chem. Biol.* **14**, 644–651 (2010).
75. K. A. Henzler-Wildman *et al.*, A hierarchy of timescales in protein dynamics is linked to enzyme catalysis. *Nature* **450**, 913 (2007).
76. E. Z. Eisenmesser *et al.*, Intrinsic dynamics of an enzyme underlies catalysis. *Nature* **438**, 117–121 (2005).
77. C. M. Cheatum, Low-frequency protein motions coupled to catalytic sites. *Annu. Rev. Phys. Chem.* **71**, 267–288 (2020).
78. R. H. Austin, K. W. Beeson, L. Eisenstein, H. Frauenfelder, I. C. Gunsalus, Dynamics of ligand binding to myoglobin. *Biochemistry* **14**, 5355–5373 (1975).
79. F. H. Arnold, Directed evolution: Bringing new chemistry to life. *Angew. Chem. Int. Ed.* **57**, 4143–4148 (2018).
80. R. Otten *et al.*, Rescue of conformational dynamics in enzyme catalysis by directed evolution. *Nat. Commun.* **9**, 1314 (2018).
81. M. Wilding, N. Hong, M. Spence, A. M. Buckle, C. J. Jackson, Protein engineering: The potential of remote mutations. *Biochem. Soc. Trans.* **47**, 701–711 (2019).
82. J. W. Schafer, S. D. Schwartz, Directed evolution's influence on rapid density fluctuations illustrates how protein dynamics can become coupled to chemistry. *ACS Catal.* **10**, 8476–8484 (2020).
83. C. J. Markin *et al.*, Revealing enzyme functional architecture via high-throughput microfluidic enzyme kinetics. *Science* **373**, eabf8761 (2021).
84. H. G. Saavedra, J. O. Wrabl, J. A. Anderson, J. Li, V. J. Hilser, Dynamic allostery can drive cold adaptation in enzymes. *Nature* **558**, 324–328 (2018).
85. M. B. Vaughn, J. Zhang, T. G. Spiro, R. B. Dyer, J. P. Klinman, Activity-related microsecond dynamics revealed by temperature-jump Förster resonance energy transfer measurements on thermophilic alcohol dehydrogenase. *J. Am. Chem. Soc.* **140**, 900–903 (2018).
86. S. J. Benkovic, G.G. Hammes, S. Hammes-Schiffer, J. P. Klinman, Free-energy landscape of enzyme catalysis. *Biochemistry* **47**, 3317–3321 (2008).
87. S.J. Benkovic *et al.*, Oscillatory active-site motions correlate with kinetic isotope effects in formate dehydrogenase. *ACS Catal.* **9**, 11199–11206 (2019).
88. D. Arnlund *et al.*, Visualizing a protein quake with time-resolved X-ray scattering at a free-electron laser. *Nat. Methods* **11**, 923–926 (2014).
89. G. Li, D. Magana, R. B. Dyer, Anisotropic energy flow and allosteric ligand binding in albumin. *Nat. Commun.* **5**, 3100 (2014).
90. T. P. Causgrove, R. B. Dyer, Picosecond structural dynamics of myoglobin following photolysis of carbon monoxide. *J. Phys. Chem.* **100**, 3273–3277 (1996).
91. D. M. Leitner, T. Yamato "Mapping energy transport networks in proteins" in *Reviews in Computational Chemistry,* A. L. Parrill, K. B. Lipkowitz, Eds. (2018), **vol. 31**, pp. 63–113.
92. D. M. Leitner, Energy flow in proteins. *Annu. Rev. Phys. Chem.* **59**, 233–259 (2008).
93. X. Yu, D. M. Leitner, Heat flow in proteins: Computation of thermal transport coefficients. *J. Chem. Phys.* **122**, 054902 (2005).
94. X. Yu, D. M. Leitner, Vibrational energy transfer and heat conduction in a protein. *J. Phys. Chem. B* **107**, 1698–1707 (2003).
95. T. Baumann *et al.*, Site-resolved observation of vibrational energy transfer using a genetically encoded ultrafast heater. *Angew. Chem. Int. Ed.* **58**, 2899–2903 (2019).
96. I. Nardecchia *et al.*, Out-of-equilibrium collective oscillation as phonon condensation in a model protein. *Phys. Rev. X* **8**, 031061 (2018).
97. L. Pauling, Nature of forces between large molecules of biological interest*. *Nature* **161**, 707–709 (1948).
98. L. Pauling, Molecular architecture and biological reactions. *Chem. Eng. News Arch.* **24**, 1375–1377 (1946).
99. J. P. Klinman, Dynamical activation of function in metalloenzymes. *FEBS Lett.* **597**, 79–91 (2022).